FRONTIERS OF PHYSICS

RESEARCH ARTICLE
Volume 19 / Issue 3 / 32204 / 2024

Cavity-enhanced metrology in an atomic spin-1 Bose–Einstein condensate

Renfei Zheng[1,2], Jieli Qin[3], Bing Chen[1], Xingdong Zhao[4,†], Lu Zhou[2,5,‡]

1 School of Physics, Hefei University of Technology, Hefei 230009, China
2 State Key Laboratory of Precision Spectroscopy, Department of Physics, School of Physics and Electronic Science, East China Normal University, Shanghai 200241, China
3 School of Physics and Materials Science, Guangzhou University, 230 Wai Huan Xi Road, Guangzhou Higher Education Mega Center, Guangzhou 510006, China
4 Department of Physics, Henan Normal University, Xinxiang 453007, China
5 Collaborative Innovation Center of Extreme Optics, Shanxi University, Taiyuan 030006, China
Corresponding authors. E-mail: †phyzhxd@gmail.com, ‡lzhou@phy.ecnu.edu.cn
Received September 29, 2023; accepted November 24, 2023

ABSTRACT

Atom interferometer has been proven to be a powerful tool for precision metrology. Here we propose a cavity-aided nonlinear atom interferometer, based on the quasi-periodic spin mixing dynamics of an atomic spin-1 Bose–Einstein condensate trapped in an optical cavity. We unravel that the phase sensitivity can be greatly enhanced with the cavity-mediated nonlinear interaction. The influence of encoding phase, splitting time and recombining time on phase sensitivity are carefully studied. In addition, we demonstrate a dynamical phase transition in the system. Around the criticality, a small cavity light field variation can arouse a strong response of the atomic condensate, which can serve as a new resource for enhanced sensing. This work provides a robust protocol for cavity-enhanced metrology.

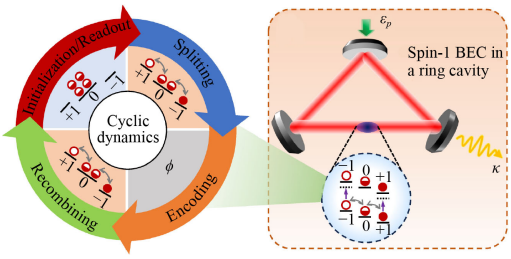

Keywords nonlinear atom interferometer, spin-1 Bose–Einstein condensate, spin-mixing dynamics, quantum Fisher information, parameter estimation

1 Introduction

Atom interferometry has become an indispensable tool for both fundamental physics research [1–7], and practical applications [8] such as gravimeters [9, 10], gradiometers [11, 12], and gyroscopes [13–15]. The unique quantum properties of ultracold atomic system provide an underlying platform to improve the sensitivity of atom interferometers beyond standard quantum limit (SQL) [16–21]. Spinor Bose–Einstein condensates (BECs) have been proven to be an ideal candidate for enhancing the sensitivity of atom interferometers beyond SQL owing to the generation of entanglements exploiting spin-exchange collisions [22, 23]. The realization of entanglement enhancement in spinor BECs through parametric amplifiers [24], spin nematic squeezing [25], and quantum phase transitions [26–28] have been demonstrated. Recently, nonlinear interferometry based on time reversal protocols was proposed in which the improvement of the signal-to-noise ratio results from amplifying the signal instead of reducing the quantum noise to circumvent low-noise detection [29–31]. Spin-exchange dynamics of spinor BECs can also be used as a nonlinear mechanism for realizing time reversal readout by controlling phase

Higher Education Press

https://doi.org/10.1007/s11467-023-1372-5

imprinting [32]. However, the difficulty of inverting the sign of Hamiltonian in an interacting many-body system with large particle numbers poses a challenge to realize time-reversed operation.

To circumvent the difficulty, a closed-cyclic nonlinear interferometer based on the quasi-periodic spin mixing dynamics in a three-mode ^{87}Rb atomic spinor condensate was proposed [33] and implemented [34]. The mechanism employs cyclic dynamics which automatically drives the system back to the vicinity of the initial state, thus bypassing time reversal operation. A nonlinear interferometer based on quasi-periodic spin mixing dynamics consists of the following processes shown in Fig. 1(a): (i) Initialization with all atoms in the $|m_F=0\rangle$ component. (ii) Splitting through creating paired atoms in $|m_F=\pm1\rangle$ components based on spin mixing dynamics with a duration time t_1. (iii) Encoding with a phase shift ϕ. (iv) Recombing with a duration time t_2. (v) Readout. When the encoded phase is $\phi=0$, the system will return back to the initial state after recombining owing to the periodic dynamics, while it evolves to another state if $\phi\neq0$. Experimentally, the nonlinear interferometer hiring cyclic dynamics has achieved a phase sensitivity of 5 decibels beyond the SQL for a large number of atoms [34]. However, the ubiquitous decoherence [35–37] will hinder the achievable phase sensitivity especially in the long evolution time required for cyclic dynamics.

In previous works [38, 39], we have studied the nonlinear dynamics by coupling the spinor condensate to an optical cavity. The nonlinear interactions between atoms and the intracavity light field provide an extra control knob for the spin mixing dynamics, giving rise to novel many body nonlinear phenomena such as strong matter wave bistability and spin domain formation. Motivated by that, here we explore the new possibility of cavity-aided atom interferometer. It has been proved that the coupling of atoms to cavity can give rise to entangled states useful in quantum metrology [40–42]. Optical cavities can be used to effectively create spin-squeezing, squeezed-state atomic clocks and highly non-classical states through interaction with atoms [43–45]. In this work, we theoretically propose a cavity-aided spin-1 nonlinear atom interferometer based on quasi-periodic spin mixing dynamics. We study the spin mixing dynamics of a spin-1 ^{87}Rb atomic condensate in a cavity and investigate the entanglement of the probe state characterized by quantum Fisher information (QFI). The results indicate that the phase sensitivity can be enhanced with cavity aiding. The influence of encoding phase, splitting time and recombining time on phase sensitivity are discussed in detail. Furthermore, we investigate that dynamical phase transition (DPT) in the cavity-condensate coupling system, which is usually defined in terms of nonanalytic behavior of a time-averaged order parameter at a critical point [46–49], can be characterized by an abrupt increase of the QFI, indicating an underlying connection to the bistable phase transition [38]. Criticality has been proved to be a useful resource for enhanced quantum sensing in a spinor condensate [50–53]. We explore the parameter estimation near the critical point with DPT, which provides a new platform for an interferometric protocol that can enable DPT for enhanced sensing.

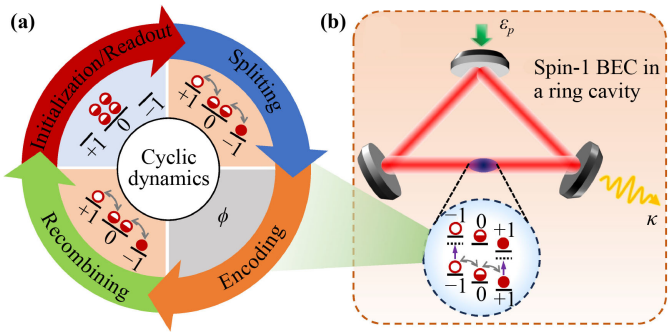

Fig. 1 **(a)** The processes based on quasi-periodic spin mixing dynamics in a spin-1 atom nonlinear interferometer: initialization, splitting, encoding, recombining and readout. **(b)** Schematic diagram for a nonlinear interferometer implemented with a spin-1 atomic condensate trapped in a unidirectional ring cavity. The cavity is driven by a coherent laser field with amplitude ε_p and decays with a rate κ. The spin exchange collisions cause a redistribution of the population among three spin components in the ground state manifold.

2 Model

We consider a model of a tightly trapped spin-1 ^{87}Rb atomic condensate trapped in a unidirectional ring cavity, as shown in Fig. 1(b). Due to the tight trapping, we can apply the single-mode approximation (SMA), under which all spin components have the same spatial wavefunction $\varphi(\boldsymbol{r})$. The cavity is driven by a coherent laser field with amplitude ε_p and frequency ω_p. The cavity mode is described by an annihilation operator $\hat{d}$, which is π-polarized and characterized by a frequency ω_c and a decay rate κ. The Hamiltonian under the SMA can be written as [38]

$$\hat{H}=\hat{H}_0+\left[U_0\left(\hat{a}_1^\dagger\hat{a}_1+\hat{a}_{-1}^\dagger\hat{a}_{-1}\right)-\delta_c\right]\hat{d}^\dagger\hat{d}+\mathrm{i}\varepsilon_p\left(\hat{d}^\dagger-\hat{d}\right), \tag{1}$$

with $\hat{H}_0$ describing the dynamics of a spin-1 condensate [54]

$$\begin{aligned}\hat{H}_0=&\lambda_a(\hat{a}_1^\dagger\hat{a}_1^\dagger\hat{a}_1\hat{a}_1+\hat{a}_{-1}^\dagger\hat{a}_{-1}^\dagger\hat{a}_{-1}\hat{a}_{-1}+2\hat{a}_0^\dagger\hat{a}_0\hat{a}_1^\dagger\hat{a}_1\\&+2\hat{a}_0^\dagger\hat{a}_0\hat{a}_{-1}^\dagger\hat{a}_{-1}-2\hat{a}_1^\dagger\hat{a}_1\hat{a}_{-1}^\dagger\hat{a}_{-1}+2\hat{a}_0^\dagger\hat{a}_0^\dagger\hat{a}_1\hat{a}_{-1}\\&+2\hat{a}_1^\dagger\hat{a}_{-1}^\dagger\hat{a}_0\hat{a}_0)+q\left(\hat{a}_1^\dagger\hat{a}_1+\hat{a}_{-1}^\dagger\hat{a}_{-1}\right),\end{aligned} \tag{2}$$

where $\hat{a}_\alpha$ $(\alpha=\pm1,0)$ is the annihilation operator associated with the condensate mode. Here $2\lambda_a=c_2\int\mathrm{d}\boldsymbol{r}\,|\varphi(\boldsymbol{r})|^4$ is the spatially integrated interaction strength with the spin-exchange interaction coefficient c_2 defined in terms

of the s-wave scattering lengths [the explicit form of c_2 is given as $c_2 = 4\pi\hbar^2(a_0 - a_2)/(3m_a)$, where m_a is the mass of each particle and a_0 (a_2) is the s wave scattering length for spin-1 atoms colliding in symmetric channels of total spin $J = 0$ ($J = 2$)]. q is the quadratic Zeeman shift. Here the magnetization $\hat{a}_1^\dagger \hat{a}_1 - \hat{a}_{-1}^\dagger \hat{a}_{-1}$ is conserved such that the linear Zeeman shift can be eliminated via a unitary transform. $\delta_c = \omega_p - \omega_c$ is the cavity-pump detuning and $U_0 = g^2/(\omega_p - \omega_a)$ is the strength of the atom–photon coupling, with g being the dipole coupling constant and ω_a the atomic transition frequency. Furthermore the photon frequency is assumed to be detuned away from the atomic transition frequency such that the atomic upper energy level can be eliminated adiabatically and the photon–atom interaction is essentially of dispersive nature. The transition selection rule allows transitions between $|F_g = 1, m_g = \pm 1\rangle$ and corresponding states in the excited manifold with the same magnetic quantum numbers $|F_e = 1, m_e = \pm 1\rangle$ while dipole transitions between $|F_g = 1, m_g = 0\rangle$ and any excited states are forbidden. On the other hand, the atomic population can be redistributed in the ground state manifold via spin exchange collisions, which is utilized to implement nonlinear splitting and recombining in the interferometer. By considering the fact that the cavity decay rate is much larger than the spin oscillation frequency, the cavity field always follows adiabatically the atomic dynamics:

$$\hat{d} = \frac{\varepsilon_p}{\kappa - \mathrm{i}\left[\delta_c - U_0\left(\hat{a}_1^\dagger \hat{a}_1 + \hat{a}_{-1}^\dagger \hat{a}_{-1}\right)\right]}. \tag{3}$$

Combining Eq. (3) and the corresponding Heisenberg equations of motion for the condensate mode operators, the effective Hamiltonian $\hat{H}_{\text{eff}}$ reads

$$\hat{H}_{\text{eff}} = \hat{H}_0 - \frac{\varepsilon_p^2}{\kappa}\arctan\left[\frac{\delta_c - U_0\left(\hat{a}_1^\dagger \hat{a}_1 + \hat{a}_{-1}^\dagger \hat{a}_{-1}\right)}{\kappa}\right]. \tag{4}$$

We anticipate that the proposed scheme can be readily implemented experimentally with recent advances in coupling a ring cavity with cold atoms [55] and BECs [56]. A mean-field treatment is adopted by replacing the operators $\hat{d}$ and $\hat{a}_\alpha$ with the corresponding c-numbers $D = \langle \hat{d} \rangle$ and $\chi_\alpha = \sqrt{N_\alpha}\exp(\mathrm{i}\theta_\alpha)$ respectively, where N_α and θ_α represent the number and the phase of internal mode α. Under this replacing, one can obtain the mean-field effective Hamiltonian as [57, 58]

$$\frac{H}{N\kappa} = \overline{q}(1 - \rho_0) + c\rho_0\left[1 - \rho_0 + \sqrt{(1-\rho_0)^2 - m^2}\cos\theta\right] + U(\rho_0), \tag{5}$$

with the normalized spin-0 population $\rho_0 = N_0/N$ and the spinor phase $\theta = \theta_1 + \theta_{-1} - 2\theta_0$. $N = N_1 + N_0 + N_{-1}$ is the total atomic number and $m = M/N$ is the atomic polarization with $M = N_1 - N_{-1}$ being the magnetization. N and M are two conserved quantities. The effective cavity-atom counterpart $U(\rho_0)$ can be derived by the equations of motion $\mathrm{d}\rho_0/\mathrm{d}\tau = -2\partial H/\partial\theta$ and $\mathrm{d}\theta/\mathrm{d}\tau = 2\partial H/\partial\rho_0$ [58] of two conjugate variables ρ_0 and θ as

$$U(\rho_0) = \eta^2 \arctan\left[\overline{U}_0(1 - \rho_0) - \overline{\delta}_c\right]/N, \tag{6}$$

where we have introduced dimensionless quantities

$$c = \frac{2N\lambda_a}{\kappa},\ \overline{q} = \frac{q}{\kappa},\ \overline{U}_0 = \frac{NU_0}{\kappa},\ \eta = \frac{\varepsilon_p}{\kappa},\ \overline{\delta}_c = \frac{\delta_c}{\kappa}.$$

3 Spin mixing dynamics

In this section, we illustrate the spin-mixing dynamics of a spin-1 ^{87}Rb atomic condensate inside a cavity in a semiclassical phase space [59], to understand the physical origin for achieving high phase sensitivity of our nonlinear interferometer. We consider a ^{87}Rb condensate of $N = 20000$ atoms confined in a cavity and a bias magnetic field fixed at 0.23 G corresponding to a quadratic Zeeman shift of $q = 2\pi \times 3.84$ Hz [34]. The atoms are prepared initially in the $|F_g = 1, m_g = 0\rangle$ hyperfine ground state (polar state). We adjust the spin-exchange interaction coefficient c_2 and the cavity decay rate κ to satisfy $\overline{q} = |c|$, at which the initial polar state undergoes a quasi-periodic oscillation [60]. Here we use the semiclassical truncated Wigner approximation (TWA) [61] to simulate the quantum dynamics (see Appendix B).

Figure 2(a) shows the evolution of ρ_0 starting from the polar state with all atoms in the $|F_g = 1, m_g = 0\rangle$ state in a spin-1 atomic condensate (solid red line) and an atom-cavity coupling system (dashed purple line). The system would not evolve in the mean-field theory due to that polar state serves as fixed point solution in both the case with and without cavity. Here the system would experience quasi-cyclic dynamics and evolve back to the vicinity of the initial state in the first period of the oscillation for both cases. The distribution in the mean field phase space of ρ_0 and θ at different evolution times are shown in Figs. 2(b)–(d) (without cavity) and Figs. 2(e)–(g) (with cavity aiding). Initially the distribution in ρ_0 is tightly packed at the top of the phase space with random spinor phase [shown in Figs. 2(b) and (e)]. As evolution proceeds, the distribution converges towards the separatrix (dashed white curve) [58] which divides the phase space into oscillating phases and winding phases [Figs. 2(c) and (f)], and disperses along the separatrix [Figs. 2(d) and (g)]. The dynamics along the separatrix is highly sensitive to perturbations, which is responsible for the high sensitivity of the nonlinear interferometer. The probability distributions of ρ_0 at intermediate evolution times are shown in Fig. 2(h) (without cavity) and (i) (with cavity aiding). One can observe a

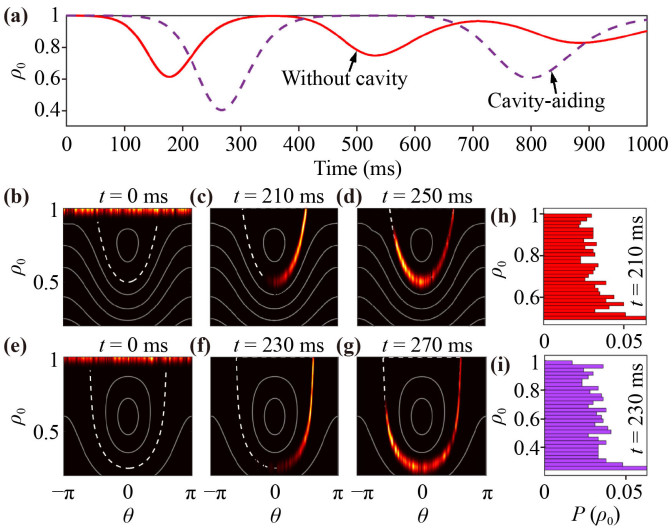

Fig. 2 **(a)** The evolution of ρ_0 starting from the polar state without cavity (solid red line) and with cavity aiding (dashed purple line). The distribution in the mean field phase space of ρ_0 and θ at different times (indicated in the panels) without cavity **(b–d)** and with cavity aiding **(e–g)**. The probability distribution of ρ_0 at corresponding times without cavity **(h)** and with cavity aiding **(i)**. The dimensionless parameters are $c=-0.002$, $\overline{U}_0=-2.5$, $\overline{\delta}_c=-1$, $\eta^2=10$.

non-Gaussian distribution for both cases. Notably, the distribution in an atom–cavity coupling system can be much broader than that in a bare atomic system, indicating enhanced entanglement resulting from cavity-mediated nonlinear interaction.

4 Phase sensitivity

The phase encoding operator is $U_p=\mathrm{e}^{\mathrm{i}\phi N_0/2}$ with $\phi=\phi_1+\phi_{-1}-2\phi_0$. Experimentally U_p is realized by quenching the quadratic Zeeman shift q to a large value with microwave dressing for a small variable time τ, and the relative phase is $\phi=2q\tau$ [34]. A nonzero phase shift will break the cyclic dynamics and make the final state phase-dependent. The phase sensitivity of the interferometer can be assessed by Gaussian error propagation as [22]

$$\Delta\phi=\Delta\rho_0/\left|\mathrm{d}\langle\rho_0\rangle/\mathrm{d}\phi\right|, \tag{7}$$

where $\langle\rho_0\rangle$ and $\Delta\rho_0$ are the mean value and the standard deviation of ρ_0 for the final state depending on splitting time t_1 and recombining time t_2.

The optimal phase sensitivity achievable is given by quantum Cramer–Rao bound $\Delta\phi_{\mathrm{QCR}}=1/\sqrt{F_Q}$, where F_Q is the quantum Fisher information (QFI) [62, 63]. The quantum Fisher information determined by the interferometer output state $\hat{\rho}(\phi)=|\psi(\phi)\rangle\langle\psi(\phi)|$ can be expressed as $F_Q[\hat{\rho}(\phi)]=\mathrm{Tr}\left[\hat{\rho}(\phi)\hat{L}_\phi^2\right]$, where $\hat{L}_\phi$ is the symmetric

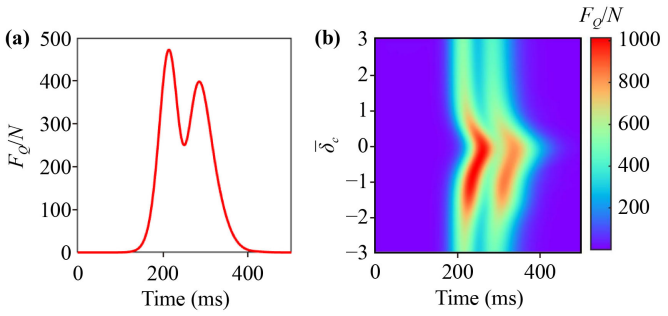

Fig. 3 **(a)** The dependence of normalized QFI F_Q/N on spin mixing time without cavity. **(b)** The normalized QFI F_Q/N as a function of spin-mixing time and cavity-pump detuning with cavity aiding. Other parameters have the same values as Fig. 2.

logarithmic derivative defined by $\partial_\phi\hat{\rho}(\phi)=\left[\hat{\rho}(\phi)\hat{L}_\phi+\hat{L}_\phi\hat{\rho}(\phi)\right]/2$ [62, 64]. For pure states $\hat{\rho}^2(\phi)=\hat{\rho}(\phi)$, we have the relation $\hat{L}_\phi=2\partial_\phi\hat{\rho}(\phi)$. Combining with the definition of the QFI, we can obtain $F_Q[\hat{\rho}(\phi)]=4[\langle\partial_\phi\psi(\phi)|\partial_\phi\psi(\phi)\rangle-|\langle\partial_\phi\psi(\phi)|\psi(\phi)\rangle|^2]$. For the output state $|\psi(\phi)\rangle=\exp(i\phi N_0/2)|\psi_p\rangle$ with a probe state $|\psi_p\rangle$, the QFI reads

$$\begin{aligned}F_Q[|\psi_p\rangle,N_0/2]&=4\left[\langle\psi_p|\left(\frac{N_0}{2}\right)^2|\psi_p\rangle-\langle\psi_p|\frac{N_0}{2}|\psi_p\rangle^2\right]\\&=(\Delta N_0)^2.\end{aligned} \tag{8}$$

For separable states, the variance of N_0 is equal to the sum of the variances for individual particles. Then the maximal variance $(\Delta N_0)^2$ is given by $N/4$ since the maximal variance of the single particle takes the value of 1/4. Therefore, the optimal phase sensitivity without quantum entanglement is given by $\Delta\phi_{\mathrm{SQL}}=2/\sqrt{N}$, which is the standard quantum limit (SQL) for a nonlinear interferometer. We estimate the phase sensitivity with metrological gain as [34]

$$G=-20\log_{10}(\Delta\phi/\Delta\phi_{\mathrm{SQL}}). \tag{9}$$

Eq. (9) indicates that higher sensitivity results in larger value of gain.

We first study the quantum Fisher information of the probe state whose entanglement property is responsible for beyond-SQL phase sensitivity. Figure 3(a) shows the normalized QFI F_Q/N of the probe state as a function of spin-mixing time in the first oscillation period without cavity. We find that the phase sensitivity is lower than the SQL ($F_Q<N/4$) for a probe state with a small evolution time. At larger times, a high phase sensitivity beyond SQL is realized. Figure 3(b) presents F_Q/N as a function of spin-mixing time and cavity-pump detuning in the first oscillation period with cavity aiding. The quantum Fisher information can obtain a larger value as compared with the bare condensate case under appropriate

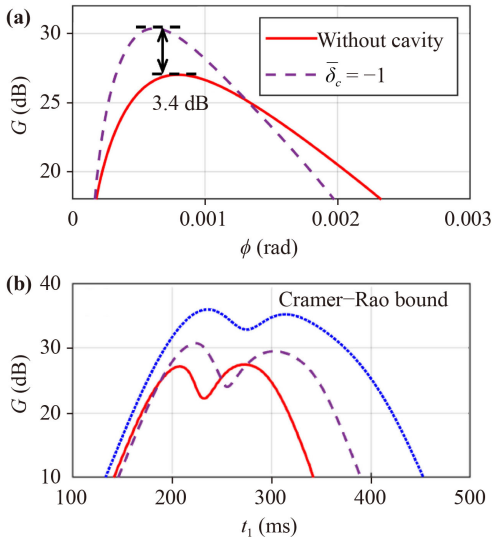

Fig. 4 **(a)** The metrological gain as a function of relative phase ϕ without cavity (solid red line) and with cavity aiding (dashed purple line). The splitting time and the total evolution time are fixed at $t_1 = 210$ ms and $t_1 + t_2 = 600$ ms for a nonlinear interferometer without cavity. The corresponding times are $t_1 = 230$ ms and $t_1 + t_2 = 670$ ms for a cavity-aided nonlinear interferometer. **(b)** The dependence of the metrological gain on splitting time t_1 without cavity (solid red line) and with cavity aiding (dashed purple line). The gains are optimized over relative phase $\phi \in [0, 0.005]$. The total evolution times have the same values as (a). The dotted blue line describes the cavity-aided metrological gain with quantum Cramer–Rao bound $\Delta\phi_{\mathrm{QCR}}$. The cavity-pump detuning is $\bar{\delta}_c = -1$. Other parameters have the same values as Fig. 2.

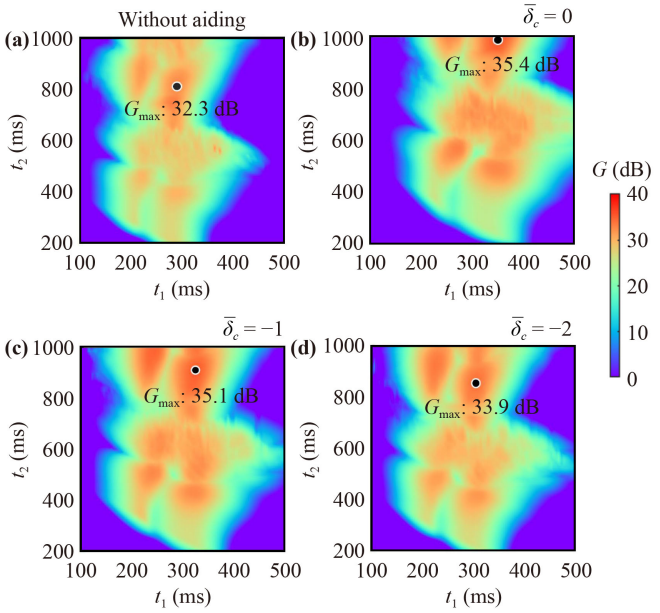

Fig. 5 The optimal metrological gain over relative phase $\phi \in [0, 0.005]$ rad as a function of t_1 and t_2 for **(a)** no cavity-aiding, **(b)** $\bar{\delta}_c = 0$, **(c)** $\bar{\delta}_c = -1$, **(d)** $\bar{\delta}_c = -2$. The maximal value of the optimal metrological gain of the nonlinear interferometer is marked by a black circle. The minimum of the colorbar denotes the optimal gain below the SQL. Other parameters have the same values as Fig. 2.

evolution time and cavity-pump detuning, indicating that phase sensitivity can be enhanced with cavity aiding.

We further explore the dependence of metrological gain of a cavity-aided nonlinear interferometer on relative phase. Figure 4(a) shows the metrological gain as a function of relative phase ϕ without cavity (solid red line) and with cavity aiding (dashed purple line). The total evolution time $t_1 + t_2$ is fixed at 600 ms (without cavity) and 670 ms (with cavity aiding) based on quasi-cyclic dynamics which drives the system back to the vicinity of the initial state [shown in Fig. 2(a)]. For a nonlinear interferometer without cavity, the splitting time t_1 is fixed at around 210 ms. While for a cavity-aided nonlinear interferometer, the splitting time t_1 is fixed at around 230 ms and the cavity-pump detuning is set as $\bar{\delta}_c = -1$. These times are chosen such that the QFIs reach the peak values (shown in Fig. 3). One can observe that the nonlinear interferometer can beat SQL for small phases (The metrological gain is zero for SQL). We found that the cavity-aided nonlinear interferometer performs better in a small range of the phase. The maximal gain of cavity-aided nonlinear interferometer can be enhanced 3.4 dB at a relative phase $\phi = 8.8 \times 10^{-4}$ rad.

The dependence of phase sensitivity in the cavity-aided nonlinear interferometer on splitting time t_1 is illustrated in Fig. 4(b), in which the metrological gain optimized over relative phase $\phi \in [0, 0.005]$ rad is presented. The solid red line and dashed purple line denote the results without cavity and with cavity aiding respectively. The total evolution time $t_1 + t_2$ is fixed at 600 ms (without cavity) and 670 ms (with cavity aiding). The optimal metrological gain can reach a higher value in the cavity-aided interferometer when choosing an appropriate splitting time, whose performance behaves more capable to saturate the Cramer–Rao bound indicated by the dotted blue line.

We also investigate the dependence of phase sensitivity of the cavity-aided nonlinear interferometer on both splitting time t_1 and recombining time t_2. The results are shown in Figure 5, in which the metrological gain optimized over relative phase $\phi \in [0, 0.005]$ rad is presented. Figure 5(a) shows the metrological gain of the nonlinear interferometer without cavity aiding, and Figs. 5(b)–(d) show the metrological gain of the cavity-aided nonlinear interferometer at $\bar{\delta}_c = 0$, $\bar{\delta}_c = -1$ and $\bar{\delta}_c = -2$. We find that the phase sensitivity is beneath the SQL for both small t_1 and t_2 and the first large metrological gain appears at both the spitting time t_1 and the recombining time t_2 around 200 ms. The maximal value of optimal metrological gain of the nonlinear interferometer is marked by a black circle. t_1 and t_2 corresponding to the

maxima gain indicate the moments at which the system develops strong entanglement during splitting and returns to the immediate vicinity of the initial polar state. The maximum metrological gain can be improved to above 3 dB. It is noticeable that due to the existence of atomic loss and technical noises, in experiment only a metrological gain below 10 dB can be achieved [34].

The cavity light field affects the sensitivity of interferometer in the sense that the photon number term $U_0|D|^2$ takes the role of an effective quadratic Zeeman energy shift, which is sensitive to the spin distribution of the condensate as indicated in Eq. (3). The entanglement builds through nonlinear cavity–atom coupling system which can help to improve the sensitivity.

5 An interferometer for an initial coherent spin state (CSS) with $\rho_0 \neq 1$

In the previous section, we focused on the case that the condensate is initially prepared in the polar state. Here we discuss the general case with the initial state prepared in an arbitrary coherent spin state (CSS) in which N spin-1 atoms point in the same direction with random spin fluctuations perpendicular to the average spin direction [65]. A CSS $|\zeta\rangle^{\otimes N}$ can be written as [66]

$$|\zeta\rangle^{\otimes N} = \frac{1}{\sqrt{N!}}\left(\zeta_1\hat{a}_1^\dagger + \zeta_0\hat{a}_0^\dagger + \zeta_{-1}a_{-1}^\dagger\right)^N|\text{vac}\rangle, \tag{10}$$

where (assuming $m = 0$)

$$\zeta = \begin{pmatrix}\zeta_1\\ \zeta_0\\ \zeta_{-1}\end{pmatrix} = \begin{pmatrix}\sqrt{\dfrac{1-\rho_0}{2}}\mathrm{e}^{\mathrm{i}\theta_1}\\ \sqrt{\rho_0}\mathrm{e}^{\mathrm{i}\theta_0}\\ \sqrt{\dfrac{1-\rho_0}{2}}\mathrm{e}^{\mathrm{i}\theta_{-1}}\end{pmatrix}. \tag{11}$$

Such a CSS can be obtained by performing a unitary transformation on a polar state $|\psi\rangle_{\text{PS}} = (N!)^{-1/2}a_0^{\dagger N}|\text{vac}\rangle$ as

$$|\zeta\rangle^{\otimes N} = \frac{1}{\sqrt{N!}}\left(\mathrm{e}^{\mathrm{i}\frac{\sigma}{2}\hat{Q}_{yz}}\hat{a}_0^\dagger\mathrm{e}^{-\mathrm{i}\frac{\sigma}{2}\hat{Q}_{yz}}\right)^N|\text{vac}\rangle, \tag{12}$$

with $\cos\sigma = \sqrt{\rho_0}$ and $\sin\sigma = \sqrt{1-\rho_0}$. The quadrapole operators are $\hat{Q}_{ij} = \hat{S}_i\hat{S}_j + \hat{S}_j\hat{S}_i - 4/3\delta_{ij}$ with $\hat{S}_i$ being the spin operator and δ_{ij} being the Kronecker delta [67]. In TWA simulation, an initial CSS is sampled by performing a unitary transformation on a polar state (see Appendix A).

We use the CSS with $\rho_0 = 0.8$, $m = 0$ and a spinor phase $\theta = -\pi$ as the initial state to study spin mixing dynamics of a cavity–condensate coupling system in the phase space. In order to clearly visualize the fluctuations in the phase space, we take the atom number of $N = 1000$. The distribution evolutions of ρ_0 starting from the CSS at different evolution times are shown in

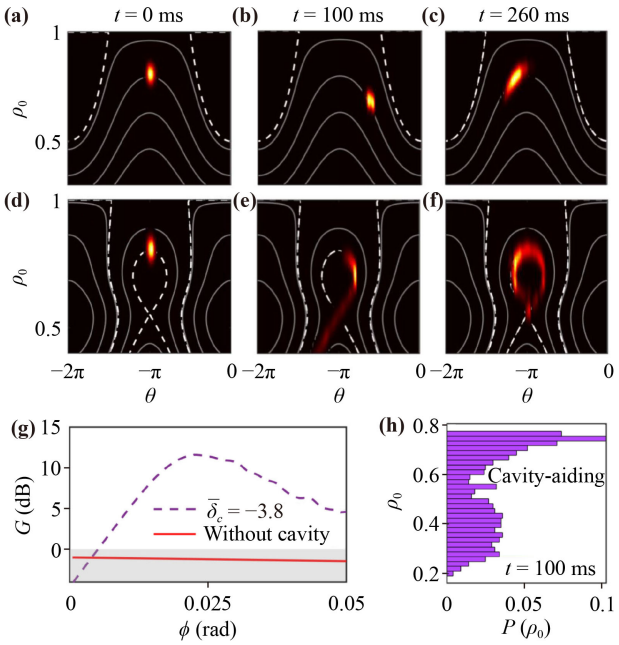

Fig. 6 The distribution evolution of ρ_0 starting from the same CSS at different evolution times (indicated in the panels) without cavity **(a–c)** and with cavity aiding **(d–f)**. **(g)** The metrological gain as a function of relative phase ϕ for the same initial CSS without cavity aiding (solid red line) and with cavity aiding (dashed purple line). The grey shaded region indicates metrological gain below the SQL. The splitting time and the total evolution time are fixed at $t_1 = 100$ ms and $t_1 + t_2 = 260$ ms. **(h)** The probability distribution of ρ_0 for a probe state at 100 ms with cavity aiding. The values of c and q are the same as Fig. 2. The cavity-related parameters are $\overline{U}_0 = -10$, $\overline{\delta}_c = -3.8$, $\eta^2 = 0.3$.

Figs. 6(a)–(c) (without cavity) and Figs. 6(d)–(f) (with cavity aiding). The cavity-related parameters are set as $\overline{U}_0 = -10$, $\overline{\delta}_c = -3.8$, $\eta^2 = 0.3$. In Figs. 6(a) and (d), the initial CSS is exhibited in the phase space as a distribution with minimal uncertainty. A major difference brought out by cavity aiding lies in that cavity-mediated nonlinearity substantially modifies the topology of the phase diagram, which makes the initial CSS reside on the separatrix and thus the dynamics becomes more sensible to perturbations. Figure 6(g) gives the metrological gain for the same initial CSS as a function of relative phase without cavity (solid red line) and with cavity aiding (dashed purple line). The total evolution time $t_1 + t_2$ and splitting time t_1 are fixed at 260 ms and 100 ms for both cases. We find that the metrological gain of the nonlinear interferometer without cavity is always beneath the SQL, while the cavity-aided interferometer can achieve a metrological gain up to 11 dB beyond the SQL. Figure 6(h) describes the probability distribution of ρ_0 at a evolution time of 100 ms with cavity aiding. One can see that the probe state shows a non-Gaussian distribution indicating the presence of entanglement.

We note that in the case of finite magnetization

$(m \neq 0)$, the principles of enhanced sensitivity would be the same as the case of $m = 0$ discussed above. The essence lies in that the system is initially prepared in a state located on the separatrix of the corresponding phase diagram, rendering its subsequent evolution sensitive to perturbations. For an arbitrary CSS, the extra knob provided by the cavity enables that one can manipulate the phase diagram topology to make the CSS a good initial testing state. The inclusion of a finite magnetization would modify the phase diagram as well, which in turn affects the interferometer sensitivity.

6 Parameter estimation harnessing dynamical phase transitions (DPT)

Our previous works have demonstrated matter wave bistability in the cavity–condensate coupling system [38, 39]. Here we explore the possibility of harnessing the dynamical phase transition (DPT) associated with bistability for parameter estimation. The mean-field bistability can be derived from the stationary solutions of mean-field dynamical equations:

$$\frac{\mathrm{d}\rho_0}{\mathrm{d}T} = 2c\rho_0\sqrt{(1-\rho_0)^2 - m^2}\sin\theta, \tag{13a}$$

$$\frac{\mathrm{d}\theta}{\mathrm{d}T} = -2\left(\overline{q} + \frac{\overline{U}_0\,|D|^2}{N}\right) + 2c\left[1 - 2\rho_0 + \frac{(1-\rho_0)(1-2\rho_0) - m^2}{\sqrt{(1-\rho_0)^2 - m^2}}\cos\theta\right], \tag{13b}$$

where $T = \kappa t$ is the dimensionless time. Here we restrict ourselves to the case with zero magnetization $m = 0$. For a ferromagnetic spinor condensate $(c < 0)$, we show the stationary solutions of ρ_0 versus cavity-pump detuning $\overline{\delta}_c$ with $\theta = 0$ in Fig. 7(a), based on a set of parameters: $c = -0.002$, $\overline{U}_0 = -5$, $\eta^2 = 0.8$, $\overline{q} = |c|$ and $N = 1000$. In the region of $-3.85 < \overline{\delta}_c < -3.47$ (marked by dashed lines), the system exhibits bistable behavior and first-order phase transition takes place within this region [38, 39].

We characterize DPT with the QFI, which is defined as the fidelity susceptibility for a tunable parameter δ_c [51, 52, 68]

$$F_Q(\delta_c, t) = -4\frac{\partial^2 F(\delta_c, \mathrm{d}\delta_c, t)}{\partial(\mathrm{d}\delta_c)^2}\bigg|_{\mathrm{d}\delta_c \to 0}, \tag{14}$$

where the fidelity $F(\delta_c, \mathrm{d}\delta_c, t) \equiv |\langle\psi(\delta_c, t)\,|\psi(\delta_c + \mathrm{d}\delta_c, t)\rangle|$ is the overlap between two dynamical states that differ by a perturbation $\mathrm{d}\delta_c$ to cavity-pump detuning, equivalent to a Loschmidt echo (LE) [69, 70] $F(\delta_c, \mathrm{d}\delta_c, t) = |\langle\psi_0|\,\mathrm{e}^{\mathrm{i}\hat{H}(\delta_c)t}\mathrm{e}^{-\mathrm{i}\hat{H}(\delta_c+\mathrm{d}\delta_c)t}\,|\psi_0\rangle|$. It measures the revival of a state $|\psi_0\rangle$ experiencing time-forward propagation under

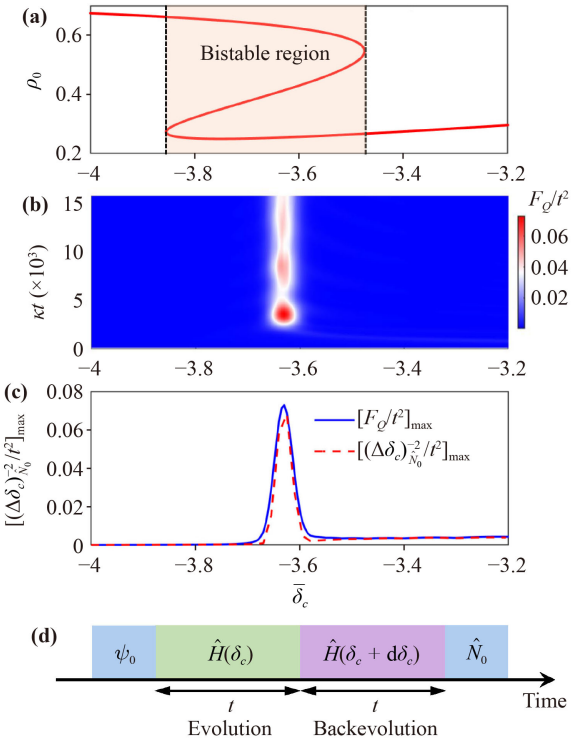

Fig. 7 **(a)** ρ_0 versus cavity detuning $\overline{\delta}_c$ for a steady-state solution with $\theta = 0$. **(b)** Time evolution of the QFI F_Q as a function of $\overline{\delta}_c$ for an initial CSS with $\rho_0 = 0.75$. **(c)** Maximum of the estimation precision $(\Delta\delta_c)^{-2}_{\tilde{N}_0}/t^2$ over time as a function of $\overline{\delta}_c$ (dashed red line). The solid blue line is for the maximum of the QFI which sets the upper bound of the precision. The parameters are $c = -0.002$, $\overline{U}_0 = -5$, $\eta^2 = 0.8$, $\overline{q} = |c|$ and $N = 1000$.

$\hat{H}(\delta_c)$ followed by reverse evolution with $\hat{H}(\delta_c + \mathrm{d}\delta_c)$. One can expect that when the system becomes critical with $\delta_c \to \delta_c^{\mathrm{cr}}$, the quantum state evolution behaves singularly and exhibits quite distinct results even for a small $\mathrm{d}\delta_c$, resulting in prominent decrease of the fidelity and a high F_Q. In order to achieve the correspondence between DPT and bistable phase transition, we take the CSS with $\rho_0 = 0.75$, $m = 0$ and $\theta = 0$ as the initial state, which is also the steady state away from the bistable region. We focus on the QFI after quenching the detuning δ_c to the bistable region to diagnose DPT. To calculate the QFI, we use the exact diagonalization method to compute the time-evolved state with eigenvector expansion (see Appendix B). The dynamical behavior of F_Q/t^2 versus δ_c is presented in Fig. 7(b), where the QFI is scaled with t^2 to absorb the expected long-time growth of $F_Q \propto t^2$ (Appendix C). Around the critical point $\overline{\delta}_c \approx -3.63$, we observe a prominent increase in the QFI. This suggests that the equilibrium phase transition can be mapped out through DPT in terms of the QFI.

In the estimation theory, the QFI sets the upper bound on the sensitivity of parameter estimation, i.e., $\Delta\delta_c \geq \sqrt{F_Q(\delta_c, t)}$. One can get access to the estimation

$(\Delta\delta_c)^{-2}$ through an observable $\hat{N}_0$ as

$$(\Delta\delta_c)^{-2}_{\hat{N}_0} = \frac{\left|\partial_{\delta_c}\langle\hat{N}_0\rangle\right|^2}{\Delta^2\hat{N}_0} \leq F_Q, \tag{15}$$

with $\Delta^2\hat{N}_0 = \langle\hat{N}_0^2\rangle - \langle\hat{N}_0\rangle^2$ representing the variance with respect to the initial CSS. Similar to the definition of the QFI in Eq. (14), the precision estimation also invokes an echo process as follows [Fig. 7(d)]: (i) Preparation of initial CSS $|\psi_0\rangle$. (ii) Evolution with the unperturbed Hamiltonian $\hat{H}(\delta_c)$ for time t. (iii) Backevolution with the perturbed Hamiltonian $\hat{H}(\delta_c + \mathrm{d}\delta_c)$ for time t. (iv) Measurement of the observable $\hat{N}_0$. To implement the echo experimentally, one needs to reverse the sign of the Hamiltonian $\hat{H}$ such that the system can experience time-reversing evolution. The sign of the Hamiltonian for a spinor condensate $\hat{H}_0$ can be varied via microwave dressing [71–73] and photon-mediated spin-exchange interaction realized through a cavity light field [74–76]. The sign of cavity–condensate coupling Hamiltonian can be manipulated through changing cavity-pump detuning δ_c and pump-atom detuning $\omega_p - \omega_a$. In Fig. 7(c), we plot the maximum of $(\Delta\delta_c)^{-2}_{\hat{N}_0}/t^2$ over time as a function of $\overline{\delta}_c$ and demonstrate that it reproduces the peak in the transient maximum of F_Q/t^2 near $\overline{\delta}_c \approx -3.63$, which identifies the DPT. It shows that the value of $(\Delta\delta_c)^{-2}_{\hat{N}_0}$ can approximately approach F_Q, which also indicates that parameter estimation can be enhanced with the onset of criticality. We demonstrate that a small perturbation in the control parameter $\mathrm{d}\delta_c$ can give rise to non-negligible variation in the observable, and this is rooted in the sensitive dependence of quantum-state evolution in the deformation of the separatrix, which is well captured through an echo process near the critical points. Our results suggest that DPTs could be harnessed for enhanced sensing by combining dynamical echoes with measurement of simple observables in nonequilibrium many-body systems.

7 Conclusion

In conclusion, we theoretically proposed a cavity-aided nonlinear atom interferometer implemented with an atomic spin-1 Bose–Einstein condensate in an optical cavity. We studied the spin mixing dynamics in this atom–cavity coupling system and the entanglement of the probe state characterized by quantum Fisher information, indicating that the phase sensitivity can be enhanced by cavity aiding. We discussed the influence of encoding phase, splitting time and recombining time on phase sensitivity and demonstrated that cavity aiding can generate a 3 dB improvement of the maximum metrological gain. Furthermore, we investigated the dynamical phase transition in this cavity–condensate coupling system which can be characterized by the quantum Fisher information via a connection to the bistable phase transition. Finally, we demonstrated an enhanced parameter estimation near the dynamical phase transition critical point, which provides a new perspective for an interferometric protocol for criticality enhanced sensing [35, 77]. It is worth noting that one can also take the counter propagating traveling cavity mode into account. In that case we expect that our main results still hold, which require further exploration. Our results not only advance the exploration of cavity-enhanced metrology but also open up new opportunities in experimental investigations in nonlinear atom interferometry and quantum precision metrology.

Declarations The authors declare that they have no competing interests and there are no conflicts.

Acknowledgements This work was supported by the National Natural Science Foundation of China (Grant Nos. 12074120 and 11904063) and the Key Scientific Research Project of Colleges and Universities in Henan Province (No. 23A140001).

Appendix A: Truncated Wigner approximation

We adopt truncated Wigner approximation to study the spin mixing dynamics of a spin-1 atomic condensate in a cavity. The Wigner function W for a quantum state approximately satisfies the equation

$$\mathrm{i}\hbar\frac{\partial W}{\partial t} \simeq \{H_W, W\}_C, \tag{A1}$$

where H_W is the Wigner–Weyl transform of the Hamiltonian, and $\{\cdots\}_C$ is the coherent state Poisson bracket. In the coherent state picture the operators $\hat{a}_\alpha$ ($\hat{a}^\dagger_\alpha$) are treated as complex c numbers χ_α (χ^*_α). Making Wigner–Weyl transform to the Heisenberg equations, we have

$$\mathrm{i}\hbar\frac{\partial\chi_\alpha}{\partial t} \simeq \{\chi_\alpha, H_W\}_C = \frac{\partial H_W}{\partial\chi^*_\alpha}. \tag{A2}$$

We initially sample the Wigner distribution W with many sets of $\{\chi_\alpha, \chi^*_\alpha\}$, and then solve the equation of motion (A2) for each set. The polar state $(N!)^{-1/2}\,a_0^{\dagger N}|\mathrm{vac}\rangle$ in the Fock basis is sampled with

$$\begin{pmatrix} \chi_1 \\ \chi_0 \\ \chi_{-1} \end{pmatrix} = \begin{pmatrix} (a+\mathrm{i}b)/2 \\ (e+f\eta)\,\mathrm{e}^{\mathrm{i}2\pi\xi} \\ (c+\mathrm{i}d)/2 \end{pmatrix}, \tag{A3}$$

where a, b, c, d, η are independent Gaussian random numbers with zero mean and unit variance, while ξ is a random number from uniform distribution in $[0,1]$, and [78]

$$e=\frac{1}{2}\sqrt{2N+1+2\sqrt{N^2+N}},\ f=\frac{1}{4e}. \tag{A4}$$

Here we sample a system with 1000 trajectories. The average and variance of mode population are obtained from the average of these trajectories, according to $\langle N_\alpha\rangle=\overline{\chi_\alpha^*\chi_\alpha}-1/2$ and $(\Delta N_\alpha)^2=(\Delta\chi_\alpha^*\chi_\alpha)^2-1/4$. A coherent spin state is obtained by using a unitary rotation

$$\begin{pmatrix} \frac{\cos\sigma+1}{2} & \frac{\sin\sigma}{\sqrt{2}} & \frac{\cos\sigma-1}{2} \\ -\frac{\sin\sigma}{\sqrt{2}} & \cos\sigma & -\frac{\sin\sigma}{\sqrt{2}} \\ \frac{\cos\sigma-1}{2} & \frac{\sin\sigma}{\sqrt{2}} & \frac{\cos\sigma+1}{2} \end{pmatrix}\begin{pmatrix}\chi_1\\ \chi_0\\ \chi_{-1}\end{pmatrix}. \tag{A5}$$

Appendix B: Exact diagonalization method

We use the exact diagonalization method to compute the time-evolved state with eigenvector expansion to simulate the quantum Fisher information in Fig. 7(b). The Hamiltonian with zero magnetization $M=0$ can be written as a tridiagonal matrix

$$\begin{aligned} H=&\left\{2\lambda_a k\left[2\left(N-2k\right)-1\right]+2qk\right\}\delta_{k,k'}\\ &-\left[\eta^2\kappa\arctan\left(\overline{\delta}_c-2\overline{U}_0k/N\right)\right]\delta_{k,k'}\\ &+2\lambda_a\left[\left(k'+1\right)\sqrt{\left(N-2k'\right)\left(N-2k'-1\right)}\right]\delta_{k,k'+1}\\ &+2\lambda_a k'\sqrt{\left(N-2k'+1\right)\left(N-2k'+2\right)}\delta_{k,k'-1}, \end{aligned} \tag{B6}$$

in the Fock basis $|N,M,k\rangle$, where k is the number of pairs of $m_g=\pm1$ atoms. The matrix has a dimension $\left[\frac{N-M}{2}+1\right]\times\left[\frac{N-M}{2}+1\right]$ (here $[\cdot]$ means taking the integer part). We diagonalize the Hamiltonian to obtain the eigenvalues and eigenvectors. The initial CSS (10) of the system can be expanded in the Fock basis $|N,M,k\rangle$ as $|\zeta\rangle^{\otimes N}=\sum_{k,M}f\left(M,k\right)|M,k\rangle$ with the coefficient

$$\begin{aligned} f\left(M,k\right)=&\sqrt{\frac{N!}{N_1!N_0!N_{-1}!}}\left(\sqrt{\frac{1-\rho_0}{2}}\right)^{2k}\left(\sqrt{\rho_0}\right)^{N-2k}\\ &\times\exp\left[\mathrm{i}\left(N_1\theta_1+N_0\theta_0+N_{-1}\theta_{-1}\right)\right]. \end{aligned} \tag{B7}$$

Appendix C: Secular approximation of the quantum Fisher information

For an estimation of an overall multiplicative factor in a Hamiltonian, one can easily obtain the quantum Fisher information. For a general parameter in a Hamiltonian, we use the identity [68]

$$\begin{aligned} &\exp\left(\mathrm{i}\hat{H}t\right)\frac{\partial}{\partial\delta_c}\exp\left(-\mathrm{i}\hat{H}t\right)\\ &=-\mathrm{i}\int_0^t\mathrm{d}t'\exp\left(\mathrm{i}\hat{H}t'\right)\frac{\partial\hat{H}}{\partial\delta_c}\exp\left(-\mathrm{i}\hat{H}t'\right)\\ &=-\mathrm{i}\hat{\mathcal{H}}_c, \end{aligned} \tag{C8}$$

where $\hat{\mathcal{H}}_c=\int_0^t\mathrm{d}t'\exp\left(\mathrm{i}\hat{H}t'\right)\hat{H}_c\exp\left(-\mathrm{i}\hat{H}t'\right)$ with

$$\hat{H}_c=-\eta^2/\left\{1+\left[\overline{\delta}_c-\frac{\overline{U}_0}{N}\left(\hat{a}_1^\dagger\hat{a}_1+\hat{a}_{-1}^\dagger\hat{a}_{-1}\right)\right]^2\right\}. \tag{C9}$$

This leads to $F_Q\left(\delta_c,t\right)=4\Delta^2\hat{\mathcal{H}}_c$. It is possible to extract a useful expression for the long-time secular behavior of the QFI using the expansion $|\psi_0\rangle=\sum_n c_n|\psi_n\rangle$, where $|\psi_n\rangle$ is the eigenstate of $\hat{H}$ with the corresponding eigenenergy E_n. One can get

$$\begin{aligned} F_Q\left(\delta_c,t\right)=&4t^2\sum_n\left|\sum_m c_m H_c^{nm}\mathrm{sinc}\left(\frac{E_{nm}t}{2}\right)\mathrm{e}^{\mathrm{i}E_{nm}t/2}\right|^2\\ &-4t^2\left|\sum_{n,m}c_n^*c_m H_c^{nm}\mathrm{sinc}\left(\frac{E_{nm}t}{2}\right)\mathrm{e}^{\mathrm{i}E_{nm}t/2}\right|^2, \end{aligned} \tag{C10}$$

with $E_{nm}=E_n-E_m$. In the long-time limit, the sinc function gives the value of 1 with $E_{nm}=0$ and zero otherwise. We assume that only the terms with $E_{nm}=0$ survive in the $t\to\infty$ limit [52] and the spectrum of $\hat{H}$ is nondegenerate, and the QFI Eq. (C10) can be approximated by

$$F_Q\left(\delta_c,t\right)\approx4t^2\left[\sum_n\left|c_n\right|^2\left|H_c^{nn}\right|^2-\left(\sum_n\left|c_n\right|^2H_c^{nn}\right)^2\right]. \tag{C11}$$

References

1. A. D. Cronin, J. Schmiedmayer, and D. E. Pritchard, Optics and interferometry with atoms and molecules, *Rev. Mod. Phys.* 81(3), 1051 (2009)
2. J. B. Fixler, G. Foster, J. McGuirk, and M. Kasevich, Atom interferometer measurement of the Newtonian constant of gravity, *Science* 315(5808), 74 (2007)
3. G. Lamporesi, A. Bertoldi, L. Cacciapuoti, M. Prevedelli, and G. M. Tino, Determination of the Newtonian gravitational constant using atom interferometry, *Phys. Rev. Lett.* 100(5), 050801 (2008)
4. P. W. Graham, J. M. Hogan, M. A. Kasevich, and S. Rajendran, New method for gravitational wave detection with atomic sensors, *Phys. Rev. Lett.* 110(17), 171102 (2013)
5. G. Rosi, F. Sorrentino, L. Cacciapuoti, M. Prevedelli, and G. Tino, Precision measurement of the Newtonian

gravitational constant using cold atoms, *Nature* 510(7506), 518 (2014)
6. W. Chaibi, R. Geiger, B. Canuel, A. Bertoldi, A. Landragin, and P. Bouyer, Low frequency gravitational wave detection with ground-based atom interferometer arrays, *Phys. Rev. D* 93(2), 021101 (2016)
7. R. H. Parker, C. Yu, W. Zhong, B. Estey, and H. Müller, Measurement of the fine-structure constant as a test of the standard model, *Science* 360(6385), 191 (2018)
8. K. Bongs, M. Holynski, J. Vovrosh, P. Bouyer, G. Condon, E. Rasel, C. Schubert, W. P. Schleich, and A. Roura, Taking atom interferometric quantum sensors from the laboratory to real-world applications, *Nat. Rev. Phys.* 1(12), 731 (2019)
9. A. Peters, K. Y. Chung, and S. Chu, Measurement of gravitational acceleration by dropping atom, *Nature* 400(6747), 849 (1999)
10. P. Altin, M. Johnsson, V. Negnevitsky, G. Dennis, R. P. Anderson, J. Debs, S. Szigeti, K. Hardman, S. Bennetts, G. McDonald, L. D. Turner, J. D. Close, and N. P. Robins, Precision atomic gravimeter based on Bragg diffraction, *New J. Phys.* 15(2), 023009 (2013)
11. M. Snadden, J. McGuirk, P. Bouyer, K. Haritos, and M. Kasevich, Measurement of the earth's gravity gradient with an atom interferometer-based gravity gradiometer, *Phys. Rev. Lett.* 81(5), 971 (1998)
12. A. Trimeche, B. Battelier, D. Becker, A. Bertoldi, P. Bouyer, C. Braxmaier, E. Charron, R. Corgier, M. Cornelius, K. Douch, N. Gaaloul, S. Herrmann, J. Müller, E. Rasel, C. Schubert, H. Wu, and F. Pereira dos Santos, Concept study and preliminary design of a cold atom interferometer for space gravity gradiometry, *Class. Quantum Gravity* 36(21), 215004 (2019)
13. F. Riehle, T. Kisters, A. Witte, J. Helmcke, and C. J. Bordé, Optical Ramsey spectroscopy in a rotating frame: Sagnac effect in a matter-wave interferometer, *Phys. Rev. Lett.* 67(2), 177 (1991)
14. T. Gustavson, P. Bouyer, and M. Kasevich, Precision rotation measurements with an atom interferometer gyroscope, *Phys. Rev. Lett.* 78(11), 2046 (1997)
15. J. Stockton, K. Takase, and M. Kasevich, Absolute geodetic rotation measurement using atom interferometry, *Phys. Rev. Lett.* 107(13), 133001 (2011)
16. H. Strobel, W. Muessel, D. Linnemann, T. Zibold, D. B. Hume, L. Pezzè, A. Smerzi, and M. K. Oberthaler, Fisher information and entanglement of non-Gaussian spin states, *Science* 345(6195), 424 (2014)
17. J. Estève, C. Gross, A. Weller, S. Giovanazzi, and M. K. Oberthaler, Squeezing and entanglement in a Bose–Einstein condensate, *Nature* 455(7217), 1216 (2008)
18. B. Lücke, M. Scherer, J. Kruse, L. Pezzé, F. Deuretzbacher, P. Hyllus, O. Topic, J. Peise, W. Ertmer, J. Arlt, L. Santos, A. Smerzi, and C. Klempt, Twin matter waves for interferometry beyond the classical limit, *Science* 334(6057), 773 (2011)
19. C. Gross, T. Zibold, E. Nicklas, J. Esteve, and M. K. Oberthaler, Nonlinear atom interferometer surpasses classical precision limit, *Nature* 464(7292), 1165 (2010)
20. Y. Zeng, P. Xu, X. He, Y. Liu, M. Liu, J. Wang, D. Papoular, G. Shlyapnikov, and M. Zhan, Entangling two individual atoms of different isotopes via Rydberg blockade, *Phys. Rev. Lett.* 119(16), 160502 (2017)
21. E. Pedrozo-Peñafiel, S. Colombo, C. Shu, A. F. Adiyatullin, Z. Li, E. Mendez, B. Braverman, A. Kawasaki, D. Akamatsu, Y. Xiao, and V. Vuletić, Entanglement on an optical atomic-clock transition, *Nature* 588(7838), 414 (2020)
22. L. Pezzè, A. Smerzi, M. K. Oberthaler, R. Schmied, and P. Treutlein, Quantum metrology with nonclassical states of atomic ensembles, *Rev. Mod. Phys.* 90(3), 035005 (2018)
23. G. Jin, Y. Liu, and L. You, Optimal phase sensitivity of atomic Ramsey interferometers with coherent spin states, *Front. Phys.* 6(3), 251 (2011)
24. J. Wrubel, A. Schwettmann, D. P. Fahey, Z. Glassman, H. Pechkis, P. Griffin, R. Barnett, E. Tiesinga, and P. Lett, Spinor Bose–Einstein-condensate phase-sensitive amplifier for $SU(1, 1)$ interferometry, *Phys. Rev. A* 98(2), 023620 (2018)
25. T. W. Mao, Q. Liu, X. W. Li, J. H. Cao, F. Chen, W. X. Xu, M. K. Tey, Y. X. Huang, and L. You, Quantum enhanced sensing by echoing spin-nematic squeezing in atomic Bose–Einstein condensate, *Nat. Phys.* 19(11), 1585 (2023)
26. X. Y. Luo, Y. Q. Zou, L. N. Wu, Q. Liu, M. F. Han, M. K. Tey, and L. You, Deterministic entanglement generation from driving through quantum phase transitions, *Science* 355(6325), 620 (2017)
27. P. Feldmann, M. Gessner, M. Gabbrielli, C. Klempt, L. Santos, L. Pezzè, and A. Smerzi, Interferometric sensitivity and entanglement by scanning through quantum phase transitions in spinor Bose–Einstein condensates, *Phys. Rev. A* 97(3), 032339 (2018)
28. Y. Q. Zou, L. N. Wu, Q. Liu, X. Y. Luo, S. F. Guo, J. H. Cao, M. K. Tey, and L. You, Beating the classical precision limit with spin-1 Dicke states of more than 10 000 atoms, *Proc. Natl. Acad. Sci. USA* 115(25), 6381 (2018)
29. E. Davis, G. Bentsen, and M. Schleier-Smith, Approaching the Heisenberg limit without single-particle detection, *Phys. Rev. Lett.* 116(5), 053601 (2016)
30. F. Fröwis, P. Sekatski, and W. Dür, Detecting large quantum Fisher information with finite measurement precision, *Phys. Rev. Lett.* 116(9), 090801 (2016)
31. T. Macrì, A. Smerzi, and L. Pezzè, Loschmidt echo for quantum metrology, *Phys. Rev. A* 94(1), 010102 (2016)
32. D. Linnemann, H. Strobel, W. Muessel, J. Schulz, R. J. Lewis-Swan, K. V. Kheruntsyan, and M. K. Oberthaler, Quantum-enhanced sensing based on time reversal of nonlinear dynamics, *Phys. Rev. Lett.* 117(1), 013001 (2016)
33. M. Gabbrielli, L. Pezzè, and A. Smerzi, Spin-mixing interferometry with Bose–Einstein condensates, *Phys. Rev. Lett.* 115(16), 163002 (2015)
34. Q. Liu, L. N. Wu, J. H. Cao, T. W. Mao, X. W. Li, S. F. Guo, M. K. Tey, and L. You, Nonlinear interferometry beyond classical limit enabled by cyclic dynamics, *Nat. Phys.* 18(2), 167 (2022)
35. W. T. He, C. W. Lu, Y. X. Yao, H. Y. Zhu, and Q. Ai, Criticality-based quantum metrology in the presence of

decoherence, *Front. Phys.* 18(3), 31304 (2023)
36. A. W. Chin, S. F. Huelga, and M. B. Plenio, Quantum metrology in non-Markovian environments, *Phys. Rev. Lett.* 109(23), 233601 (2012)
37. M. Jarzyna and R. Demkowicz-Dobrzański, True precision limits in quantum metrology, *New J. Phys.* 17(1), 013010 (2015)
38. L. Zhou, H. Pu, H. Y. Ling, and W. Zhang, Cavity-mediated strong matter wave bistability in a spin-1 condensate, *Phys. Rev. Lett.* 103(16), 160403 (2009)
39. L. Zhou, H. Pu, H. Y. Ling, K. Zhang, and W. Zhang, Spin dynamics and domain formation of a spinor Bose–Einstein condensate in an optical cavity, *Phys. Rev. A* 81(6), 063641 (2010)
40. A. Kuzmich, L. Mandel, and N. P. Bigelow, Generation of spin squeezing via continuous quantum nondemolition measurement, *Phys. Rev. Lett.* 85(8), 1594 (2000)
41. A. Kuzmich, L. Mandel, J. Janis, Y. Young, R. Ejnisman, and N. Bigelow, Quantum nondemolition measurements of collective atomic spin, *Phys. Rev. A* 60(3), 2346 (1999)
42. A. Kuzmich and E. S. Polzik, Atomic continuous variable processing and light-atoms quantum interface, in: Quantum Information with Continuous Variables, Springer, pp 231–265, 2003
43. R. Miller, T. Northup, K. Birnbaum, A. Boca, A. Boozer, and H. Kimble, Trapped atoms in cavity QED: Coupling quantized light and matter, *J. Phys. At. Mol. Opt. Phys.* 38(9), S551 (2005)
44. H. Ritsch, P. Domokos, F. Brennecke, and T. Esslinger, Cold atoms in cavity-generated dynamical optical potentials, *Rev. Mod. Phys.* 85(2), 553 (2013)
45. H. Tanji-Suzuki, I. D. Leroux, M. H. Schleier-Smith, M. Cetina, A. T. Grier, J. Simon, and V. Vuletić, Interaction between atomic ensembles and optical resonators: Classical description, in: Advances in Atomic, Molecular, and Optical Physics, Vol. 60, Elsevier, pp 201–237, 2011
46. M. Eckstein, M. Kollar, and P. Werner, Thermalization after an interaction quench in the Hubbard model, *Phys. Rev. Lett.* 103(5), 056403 (2009)
47. A. Gambassi and P. Calabrese, Quantum quenches as classical critical films, *Europhys. Lett.* 95(6), 66007 (2011)
48. P. Smacchia, M. Knap, E. Demler, and A. Silva, Exploring dynamical phase transitions and prethermalization with quantum noise of excitations, *Phys. Rev. B* 91(20), 205136 (2015)
49. J. Lang, B. Frank, and J. C. Halimeh, Concurrence of dynamical phase transitions at finite temperature in the fully connected transverse-field Ising model, *Phys. Rev. B* 97(17), 174401 (2018)
50. S. S. Mirkhalaf, E. Witkowska, and L. Lepori, Supersensitive quantum sensor based on criticality in an antiferromagnetic spinor condensate, *Phys. Rev. A* 101(4), 043609 (2020)
51. S. S. Mirkhalaf, D. B. Orenes, M. W. Mitchell, and E. Witkowska, Criticality-enhanced quantum sensing in ferromagnetic Bose–Einstein condensates: Role of readout measurement and detection noise, *Phys. Rev. Lett.* 103(2), 023317 (2021)
52. Q. Guan and R. J. Lewis-Swan, Identifying and harnessing dynamical phase transitions for quantum-enhanced sensing, *Phys. Rev. Res.* 3(3), 033199 (2021)
53. L. Zhou, J. Kong, Z. Lan, and W. Zhang, Dynamical quantum phase transitions in a spinor Bose–Einstein condensate and criticality enhanced quantum sensing, *Phys. Rev. Res.* 5(1), 013087 (2023)
54. C. Law, H. Pu, and N. Bigelow, Quantum spins mixing in spinor Bose–Einstein condensates, *Phys. Rev. Lett.* 81(24), 5257 (1998)
55. B. Megyeri, G. Harvie, A. Lampis, and J. Goldwin, Directional bistability and nonreciprocal lasing with cold atoms in a ring cavity, *Phys. Rev. Lett.* 121(16), 163603 (2018)
56. S. C. Schuster, P. Wolf, D. Schmidt, S. Slama, and C. Zimmermann, Pinning transition of Bose–Einstein condensates in optical ring resonators, *Phys. Rev. Lett.* 121(22), 223601 (2018)
57. S. Yi, Ö. Müstecaplıoğlu, C. P. Sun, and L. You, Single mode approximation in a spinor-1 atomic condensate, *Phys. Rev. A* 66(1), 011601 (2002)
58. W. Zhang, D. Zhou, M. S. Chang, M. Chapman, and L. You, Coherent spin mixing dynamics in a spin-1 atomic condensate, *Phys. Rev. A* 72(1), 013602 (2005)
59. C. Gerving, T. Hoang, B. Land, M. Anquez, C. Hamley, and M. Chapman, Non-equilibrium dynamics of an unstable quantum pendulum explored in a spin-1 Bose–Einstein condensate, *Nat. Commun.* 3(1), 1169 (2012)
60. M. S. Chang, Q. Qin, W. Zhang, L. You, and M. S. Chapman, Coherent spinor dynamics in a spin-1 Bose condensate, *Nat. Phys.* 1(2), 111 (2005)
61. P. B. Blakie, A. Bradley, M. Davis, R. Ballagh, and C. Gardiner, Dynamics and statistical mechanics of ultracold Bose gases using *c*-field techniques, *Adv. Phys.* 57(5), 363 (2008)
62. C. W. Helstrom, Minimum mean-squared error of estimates in quantum statistics, *Phys. Lett. A* 25(2), 101 (1967)
63. S. L. Braunstein and C. M. Caves, Statistical distance and the geometry of quantum states, *Phys. Rev. Lett.* 72(22), 3439 (1994)
64. A. S. Holevo, Probabilistic and Statistical Aspects of Quantum Theory, Vol. 1, Springer Science & Business Media, 2011
65. W. M. Zhang, D. H. Feng, and R. Gilmore, Coherent states: Theory and some applications, *Rev. Mod. Phys.* 62(4), 867 (1990)
66. E. Yukawa, M. Ueda, and K. Nemoto, Classification of spin-nematic squeezing in spin-1 collective atomic systems, *Phys. Rev. A* 88(3), 033629 (2013)
67. C. D. Hamley, C. Gerving, T. Hoang, E. Bookjans, and M. S. Chapman, Spin-nematic squeezed vacuum in a quantum gas, *Nat. Phys.* 8(4), 305 (2012)
68. S. Pang and T. A. Brun, Quantum metrology for a general Hamiltonian parameter, *Phys. Rev. A* 90(2), 022117 (2014)
69. A. Goussev, R. A. Jalabert, H. M. Pastawski, and D. A. Wisniacki, Loschmidt echo and time reversal in complex systems, *Philos. Trans. R. Soc. A* 374(2069), 20150383 (2016)
70. T. Gorin, T. Prosen, T. H. Seligman, and M. Žnidarič,

Dynamics of Loschmidt echoes and fidelity decay, *Phys. Rep.* 435(2-5), 33 (2006)

71. F. Gerbier, A. Widera, S. Fölling, O. Mandel, and I. Bloch, Resonant control of spin dynamics in ultracold quantum gases by microwave dressing, *Phys. Rev. A* 73(4), 041602 (2006)
72. S. Leslie, J. Guzman, M. Vengalattore, J. D. Sau, M. L. Cohen, and D. Stamper-Kurn, Amplification of fluctuations in a spinor Bose–Einstein condensate, *Phys. Rev. A* 79(4), 043631 (2009)
73. P. Kunkel, M. Prüfer, H. Strobel, D. Linnemann, A. Frölian, T. Gasenzer, M. Gärttner, and M. K. Oberthaler, Spatially distributed multipartite entanglement enables EPR steering of atomic clouds, *Science* 360(6387), 413 (2018)
74. E. J. Davis, G. Bentsen, L. Homeier, T. Li, and M. H. Schleier-Smith, Photon-mediated spin-exchange dynamics of spin-1 atoms, *Phys. Rev. Lett.* 122(1), 010405 (2019)
75. M. A. Norcia, R. J. Lewis-Swan, J. R. Cline, B. Zhu, A. M. Rey, and J. K. Thompson, Cavity-mediated collective spin exchange interactions in a strontium superradiant laser, *Science* 361(6399), 259 (2018)
76. S. J. Masson, M. Barrett, and S. Parkins, Cavity QED engineering of spin dynamics and squeezing in a spinor gas, *Phys. Rev. Lett.* 119(21), 213601 (2017)
77. D. S. Ding, Z. K. Liu, B. S. Shi, G. C. Guo, K. Mølmer, and C. S. Adams, Enhanced metrology at the critical point of a many-body Rydberg atomic system, *Nat. Phys.* 18(12), 1447 (2022)
78. M. Olsen and A. Bradley, Numerical representation of quantum states in the positive-P and Wigner representations, *Opt. Commun.* 282(19), 3924 (2009)